Supplementary information

Towards an Active Droplet-Based Microfluidic Platform for Programmable Fluid Handling

Xiaobao Cao,[a,b,#] Tomas Buryska,[b,#] Tianjin Yang,[b, c] Jing Wang,[d] Peter Fischer,[e] Aaron Streets[f], Stavros Stavrakis[b*] and Andrew deMello[b*]

(a) Guangzhou Laboratory, Guangzhou International Bio Island, Guangzhou, Guangdong Province, China. (b) Institute for Chemical and Bioengineering, ETH Zürich, 8093 Zürich, Switzerland. (c) Department of Biochemistry, University of Zurich, 8057 Zurich, Switzerland. (d) Institute of Environmental Engineering, ETH Zürich, 8093, Zürich, Switzerland. (e) IFNH Food Process Engineering Group, ETH Zürich, 8092, Zürich, Switzerland. (f) Department of Bioengineering, University of California, Berkeley, California, United States of America

[1] These authors contributed equally to the work.

[*] E-Mail: stavros.stavrakis@chem.ethz.ch, andrew.demello@chem.ethz.ch

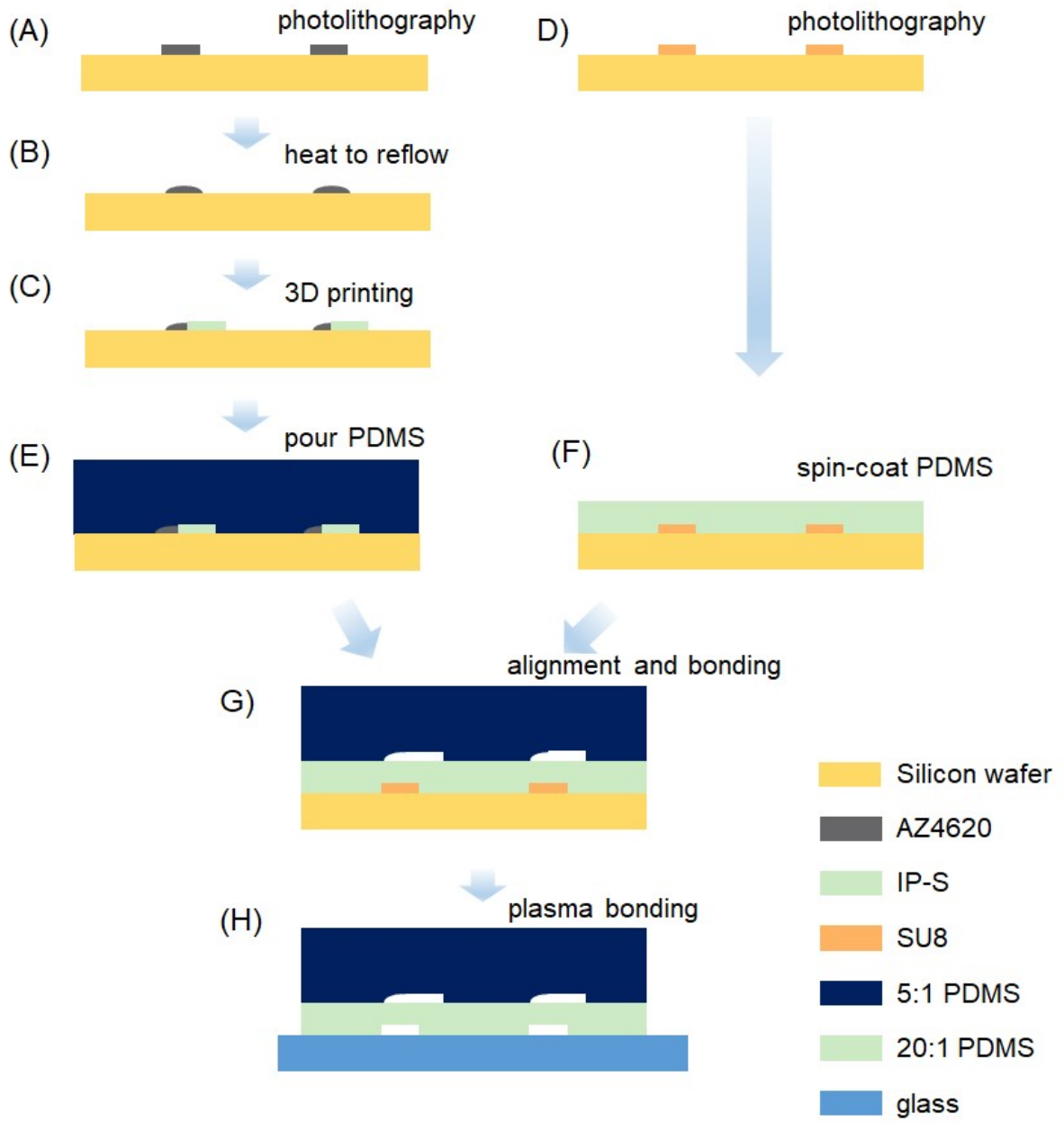

Figure S1. **Microfluidic device fabrication process.** The microfluidic device is composed of two layers: the fluidic channel layer and the control channel layer. (A)-(B) The mold for the fluidic channel layer, not including the storage chamber array and the electrode channels, was fabricated using an AZ4620 photoresist and following standard lithography procedures. (C) The storage chamber array and the electrode channels were fabricated using two photon polymerization 3-D printing. (D) The mold for the control channels was fabricated using an SU8 photoresist following standard lithography procedures. (E) A 5:1 mixture of PDMS monomer to curing agent is poured onto the fluidic channel mold and peeled off after baking for 20 minutes at 70°C. (F) A 20:1 mixture of PDMS monomer to curing agent was spin coated at 2600 rpm onto the control channel mold for 40 seconds and then baked at 70°C for 30 minutes. (G) The fluidic channel layer was then aligned with the control layer structures under a stereoscope and cured for 4 hours at 70°C. (H) The final PDMS device was plasma bonded to a glass slide after plasma treatment of both surfaces.

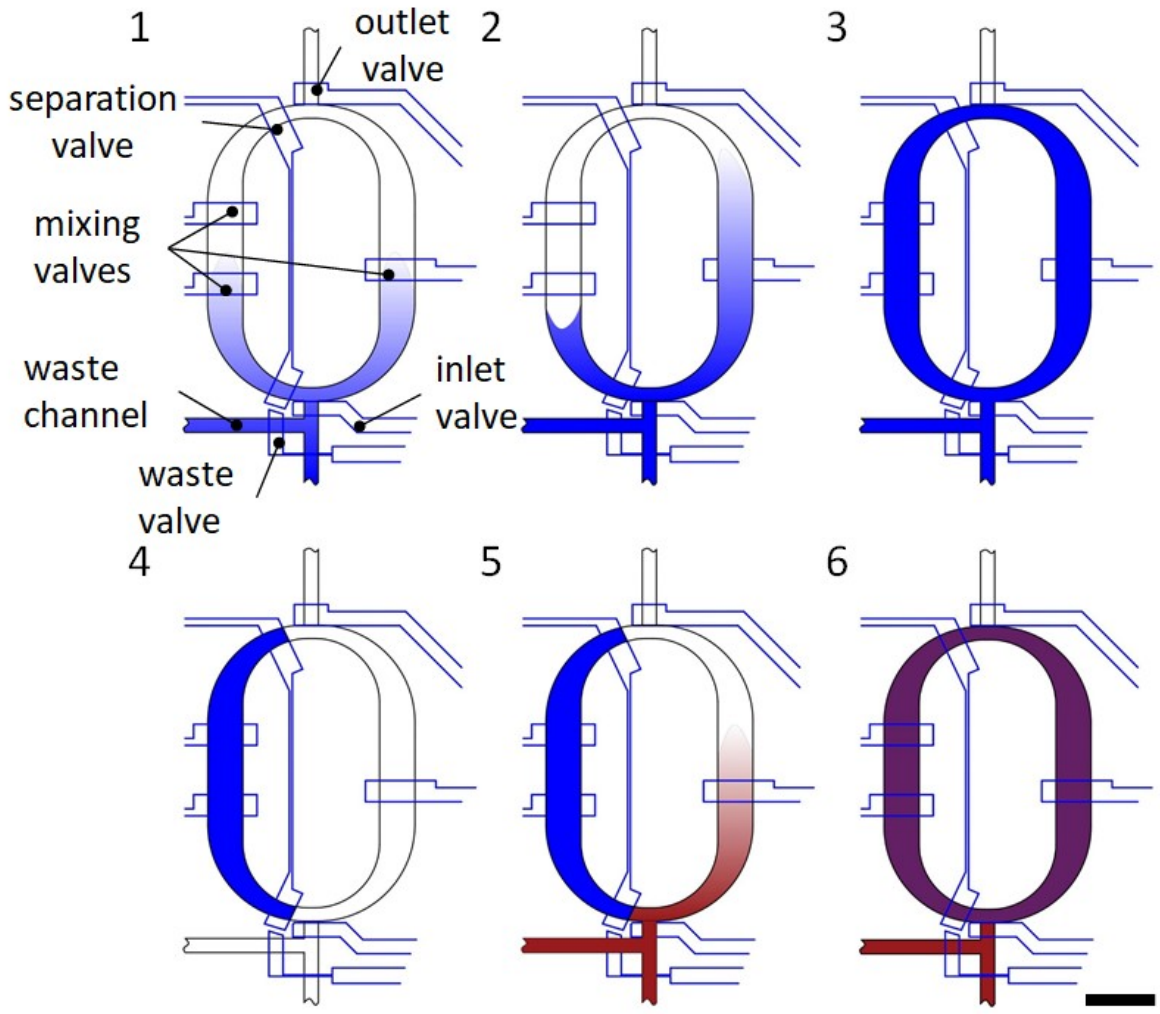

Figure S2. **Mixing ring operation during formulation**. The access valve is opened during steps 1 and 2, and a sample solution (blue) is introduced. In step 3 the mixing ring is isolated, and actuation of the mixing valves ensures complete dispersion of the sample within the ring volume. In step 4, the separation valve is closed, blocking just under half of the ring-contained fluid. The other half of the ring is purged to the outlet channel. In step 5, a secondary sample solution (red) is introduced after a user-defined number of injection steps. In step 6, the mixing ring is isolated from inlet and outlet channels and mixing valves are actuated until the final solution is fully mixed. Scale bar: 500 μm

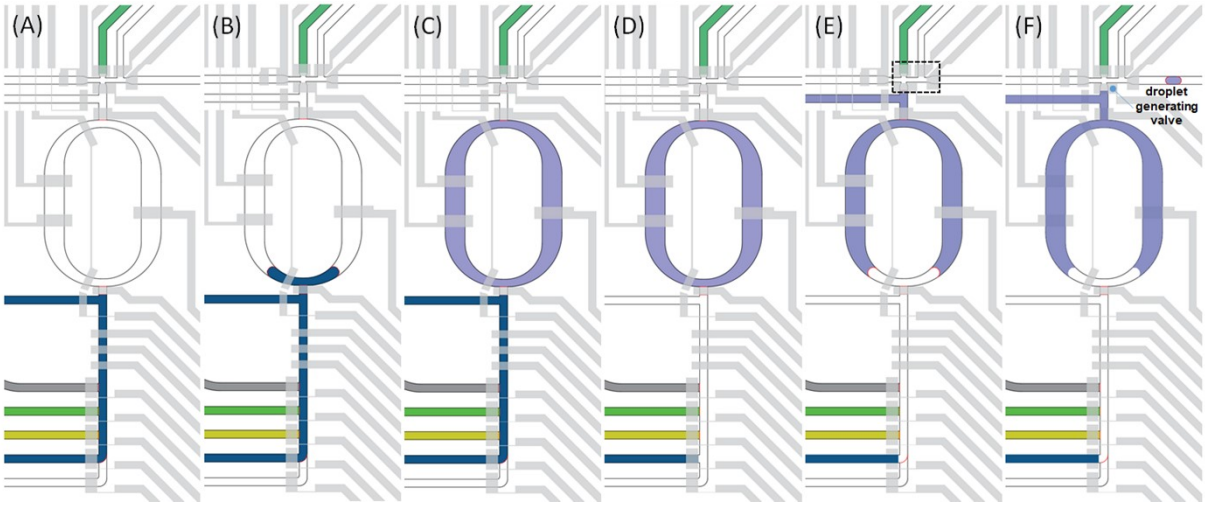

Figure S3. **Mixing ring manipulation and droplet generation**. (A) The mixing ring initially contains water. (B) A sample valve is opened, and a sample fluid (dark blue) is pumped into the mixing ring. (C) All access valves to the ring are closed and mixing is initiated by actuation of mixing valves. (D) the sample inlet channel is washed with buffer. (E) The outlet valve is opened, and the formulated solution is pumped into the droplet generation section highlighted by the dotted box. (F) The "droplet generating valve" is opened for 100 ms, allowing the formulated solution to enter the incoming oil flow to form a droplet. The droplet is subsequently transported to the storage array.

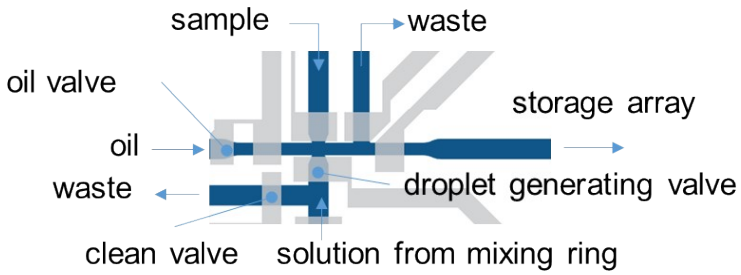

Figure S4. The droplet formation process. The mixing ring integrates a three-valve peristaltic pump, which is used to deliver defined volumes of reagents to the droplet generator. The fluid displaced from the mixing ring enters the main channel containing an oil flow and begins to form a droplet. The minimum volume of a formed droplet is controlled by the time that the droplet-generating valve is open. Accordingly, the droplet is allantoid in shape, with length longer than its cross-sectional diameter, and is separated from the channel walls by a thin film of the carrier oil.

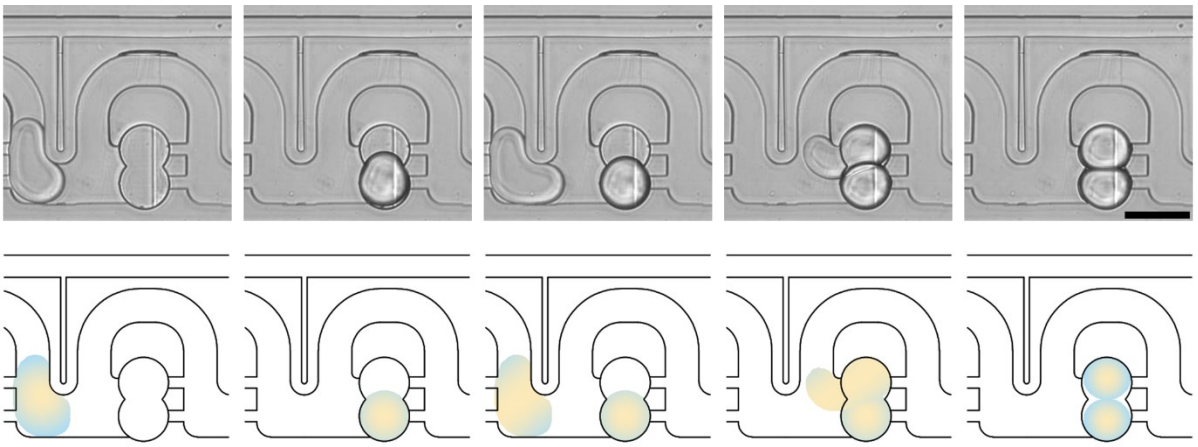

Figure S5. Filling of the droplet storage chamber. Brightfield images (upper) and corresponding schematics (bottom) illustrate the process of droplet loading into the droplet storage array. An initial incoming droplet locates itself at the bottom part of the droplet trap, where pressure resistance is the lowest. A subsequent droplet locates in the upper empty part of the droplet trap, since the bottom position is now occupied. When the storage chamber is fully occupied, any subsequent droplet incoming droplet will take the path of least resistance, which is towards the next free storage chamber. Scale bar: 100 μm.

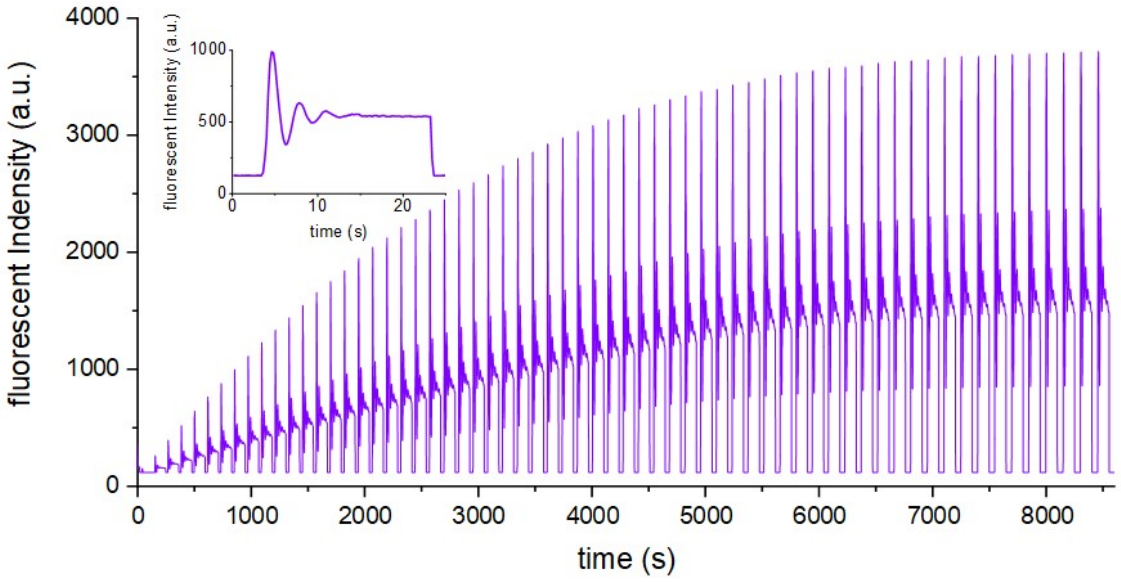

Figure S6. **An automated dilution series**. Variation of fluorescence intensity as a function of time, depicting 80 different FITC concentrations sequentially formulated inside the mixing ring. Each formulation (i.e. FITC concentration) was produced using one injection step, and thus 80 different concentrations were generated by performing 80 injection steps from a FITC stock solution. Inset: An initial rapid increase in fluorescence is followed by fluctuations caused by the mixing of the input fluids in the mixing. Complete mixing is achieved by after 300 mixing cycles (approximately 8 seconds).

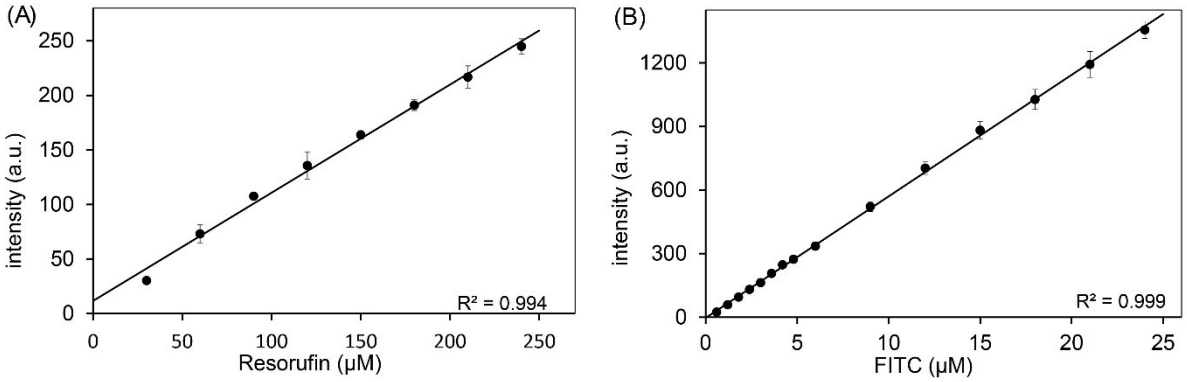

Figure S7. **Calibration curves for Resorufin (A) and FITC (B)**. In each plot, fluorescence signals were acquired from stored droplets containing serial dilutions of each individual stock dye solution. Data were measured in triplicate, with the error bars representing standard deviation values.

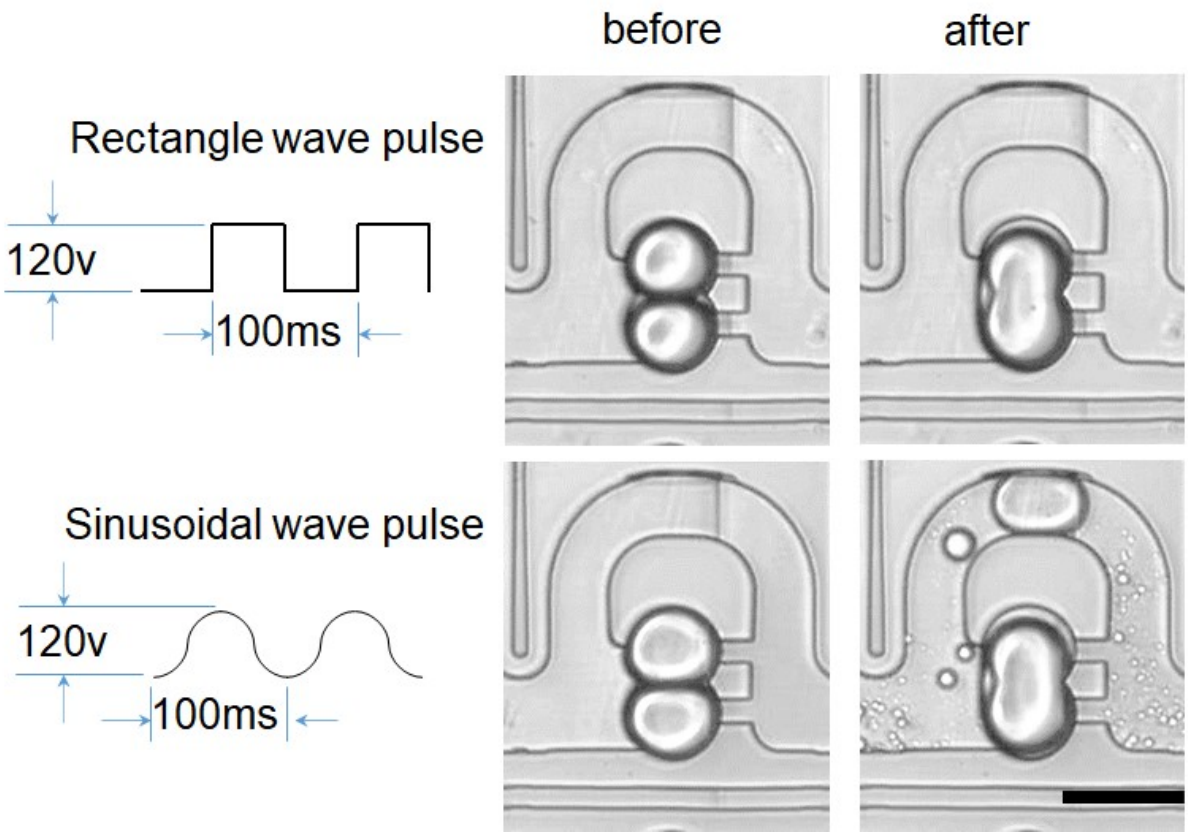

Figure S8. **Selected frames from the fusion process of two equal-sized droplets**. Square wave (upper panel) and sinusoidal (bottom panel) wave functions were applied for the droplet merging process. Please note in the case of the sinusoidal wave function, satellite droplets are created during the process of droplet fusion. The settings of the square wave voltage were: 10 kHz for 100 cycles at 120 V applied voltage. Scale bar: 100 µm.

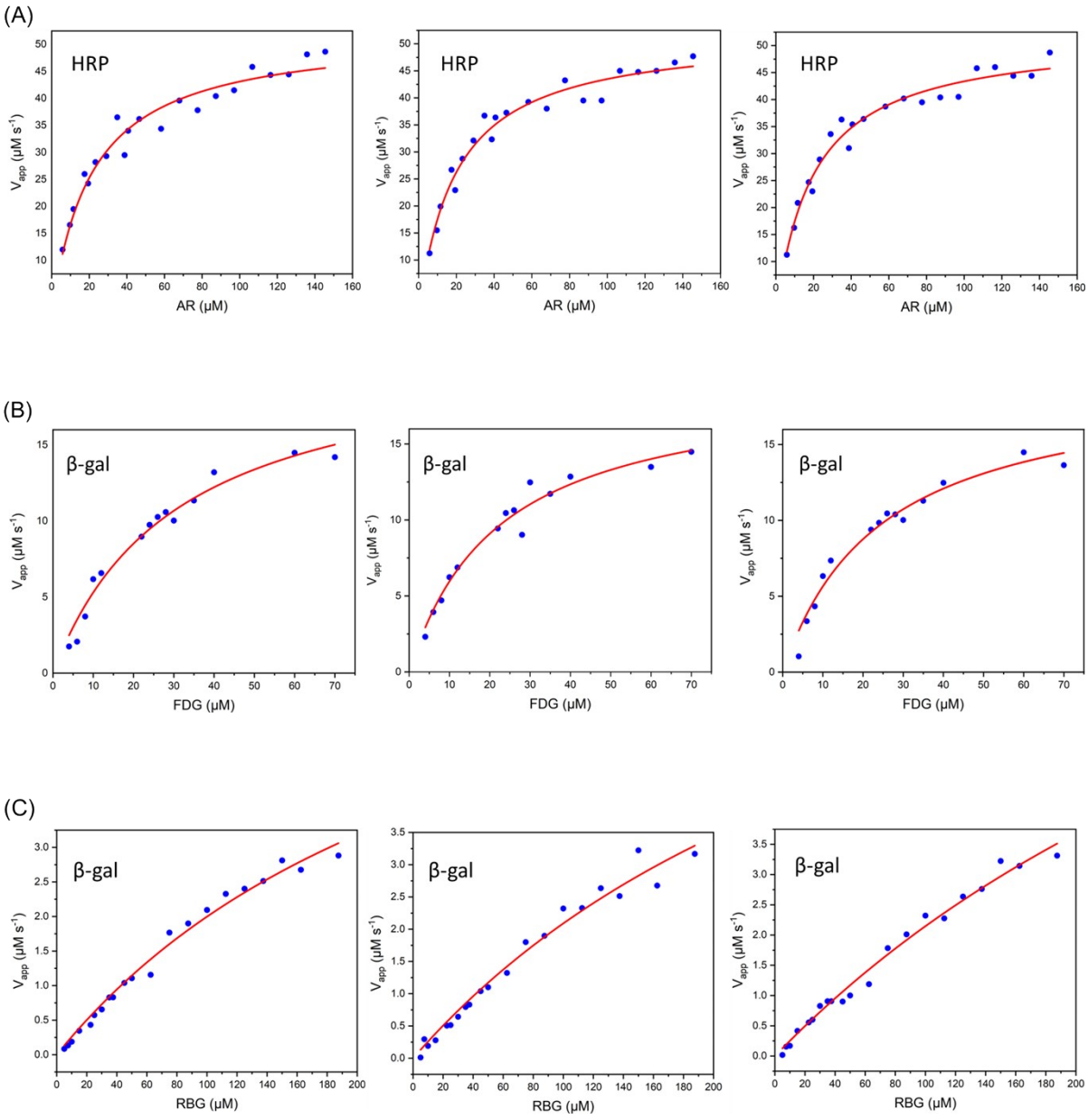

Figure S9. Michaelis-Menten kinetic plots for HRP and beta-galactosidase catalysed reactions. Three replicate measurements are depicted for the enzymatic reactions of HRP with Amplex Red, and beta-galactosidase (β-gal) with fluorescein di-b-D-galactopyranoside (FDG) and Resorufin-b-D-galactopyranoside (RBG).

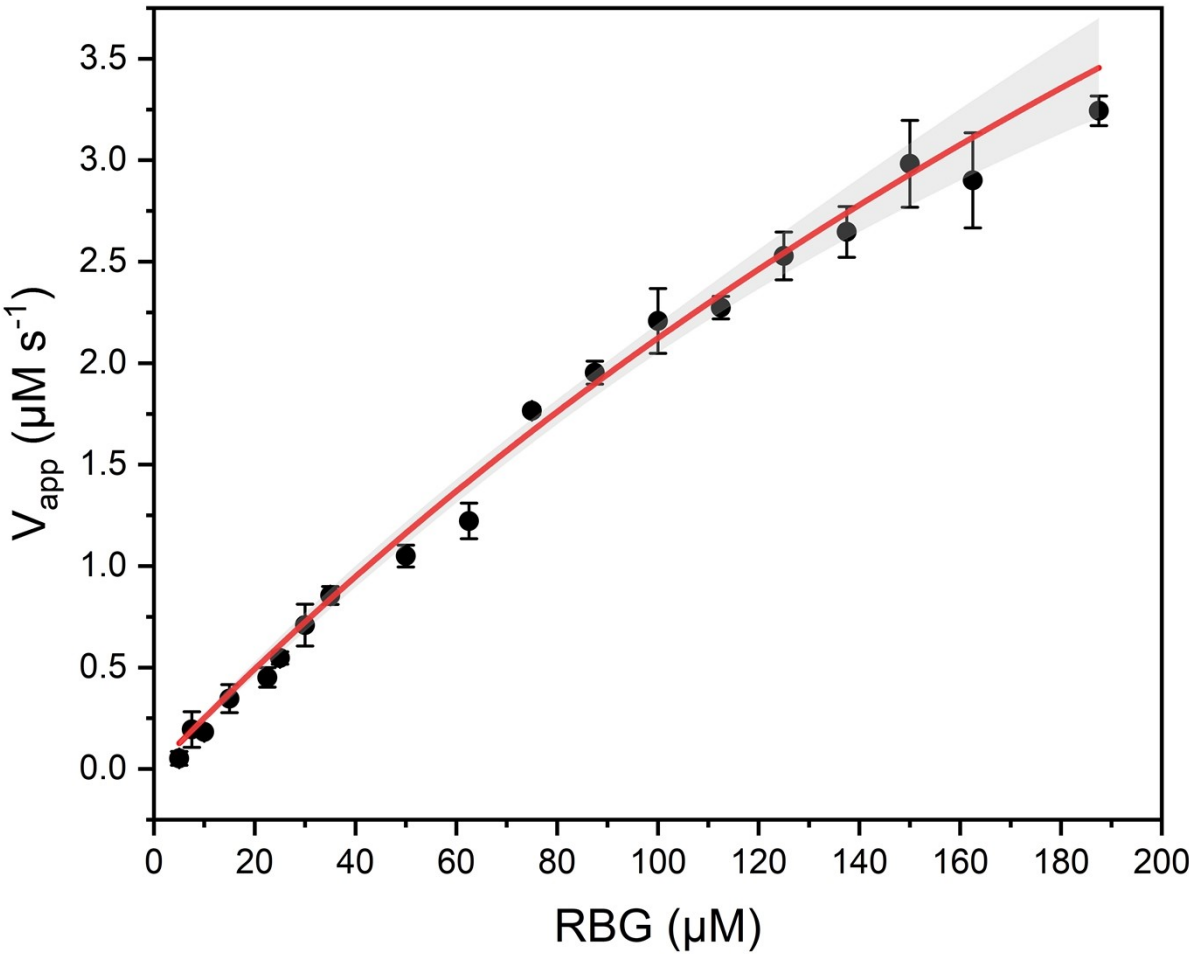

Figure S10. Michaelis-Menten plot of beta-galactosidase towards Resorufin-beta-galactopyranoside. Extracted kinetic parameters (K_m = 408 ± 66.5 μM and k_{cat} 58 ± 7.2 s^{-1}) are in good agreement with previously reported parameters: e.g. K_m = 333 ± 130 μM and k_{cat} = 64 ± 8 s^{-1}.[1] Data were measured in triplicate, with the error bars representing one standard deviation.

Table S1: Evaluation of global fit data to identify the most probable inhibition model. The data were analysed using competitive, uncompetitive and non-competitive inhibition models. Two statistical approaches weighting the residuals were employed, the Akaike Information Criterion (AIC) and the Bayesian Information Criteria (BIC) test. The lower the value, the better the fit and the higher the probability of a correct model. In both cases the lowest value is seen for the competitive inhibition model, which is in a good agreement with literature.[2]

Model	AIC	BIC
Competitive Inhibition	72.5	79.8
Uncompetitive Inhibition	94.3	112.3
Non-competitive Inhibition	111.1	118.5

Enzyme inhibition kinetic models: Competitive/Non-competitive/Uncompetitive

$$v_{app} = V_{max}S/\left(K_M\left(1 + I_c/K_i\right) + S\right) \quad \textbf{(1)}$$

$$v_{app} = V_{max}S/\left(\left(K_M + S\right)\left(1 + I_c/K_i\right)\right) \quad \textbf{(2)}$$

$$v_{app} = V_{max}S/\left(\left(K_M/1 + I_c/K_i\right) + S\right)\left(1 + I_c/K_i\right) \quad \textbf{(3)}$$

wherev_{app} is the initial reaction velocity, V_{max} is the maximum reaction velocity, S is the substrate concentration, K_M represents the Michaelis-Menten constant, I_c stands for inhibitor concentration while K_i is the inhibition constant.

REFERENCES

1. Xie, Y.; Ahmed, D.; Lapsley, M. I.; Lin, S.-C. S.; Nawaz, A. A.; Wang, L.; Huang, T. J., Single-Shot Characterization of Enzymatic Reaction Constants Km and kcat by an Acoustic-Driven, Bubble-Based Fast Micromixer. Anal. Chem., 2012, 84, 7495-7501.
2. D.H., Rob, B., Dugdale, M.L., Rahimzadeh, N., Giang, C., Lee, M., Matthews, B.W. and Huber, R.E., Direct and indirect roles of His-418 in metal binding and in the activity of β-galactosidase (E. coli). Prot. Sci., 2009, 18, 1281-1292.